THE JOURNAL OF PHYSICAL CHEMISTRY B

Article

pubs.acs.org/JPCB

# Device Physics and Operation of Lateral Bulk Heterojunction Devices

Christopher J. Lombardo,*[,†] Eric L. Danielson,[†] Micah S. Glaz,[‡] Zi-En Ooi,[§] David A. Vanden Bout,[‡] and Ananth Dodabalapur*[,†]

[†]Microelectronics Research Center, The University of Texas at Austin, Austin, Texas 78758, United States

[‡]Department of Chemistry and Biochemistry, The University of Texas at Austin, Austin, Texas 78712, United States

[§]Institute for Materials Research and Engineering (IMRE), Agency for Science, Technology, and Research (A*STAR), Singapore 117602, Republic of Singapore

**ABSTRACT:** Measurements of lateral bulk heterojunction (BHJ) devices have recently been reported as a means to characterize charge transport and recombination properties within organic photovoltaic (OPV) materials. These structures allow for the direct measurement of the lateral extents of the space charge regions, potential and electric field profiles, current versus voltage characteristics, and other physical and chemical properties. This article describes numerical simulations that show three different transport regimes present within lateral BHJ devices and two different experimental methods, which verify those findings. These measurement techniques utilize typical confocal microscopy tools as well as steady-state current versus voltage measurements on high aspect ratio nanofabricated structures in order to probe the material properties between the electrodes. Experimental results show that the lateral extents of space charge regions within these devices are approximately 1−5 $\mu$m, which are related to the drift lengths of the charge carriers, and that the mechanism of bimolecular recombination is shown to be a bulk material property. The results within this article describe a series of methods to evaluate charge transport and recombination along the in-plane direction in BHJ films and provide complementary insights to those obtained from vertical-device-based measurements.

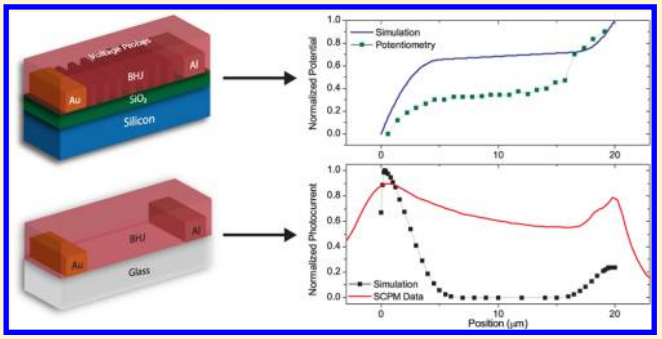


## 1. INTRODUCTION

Bulk heterojunctions (BHJs) are complex mixtures of materials, and new tools are needed to sort out the interplay of morphology and materials properties, such as recombination rate constants, carrier mobilities, and drift lengths. Researchers have typically focused on measurements on vertical solar cell devices using several methods, including time-of-flight,[1,2] photogenerated charge extraction in a linearly increasing voltage (photo-CELIV),[3,4] transient photovoltage/photocurrent,[5,6] impedance spectroscopy,[7,8] and time-resolved microwave conductivity.[9,10] These measurement methods have been very successfully employed by many research groups. Our focus has been to develop techniques that provide transport and recombination information in the lateral direction so as to yield complementary information to that obtained from the vertical-device-based measurements. Some insights obtained from our measurements are likely to help obtain a more detailed understanding of bulk heterojunction measurements. The schematic structure of a lateral BHJ device is illustrated in Figure 1. Lateral devices allow for probing the materials' properties between the electrodes using various analytical techniques. Furthermore, the electrode distances can be varied with length scales ranging from 10s of nm to more than 100s of $\mu$m, allowing for the use of spectroscopic and microscopic tools to directly probe charge carriers along the transport direction, which are not easily accessible in a vertical OPV cell because the active layer is buried beneath metal layers and/or transport layers. Additionally, because the electrodes are arranged laterally, it is possible to directly interrogate the material as a function of distance between the electrodes. Although the geometry and direction of current flow in lateral BHJ devices are different from those of vertical OPV devices, the carrier transport and recombination parameters investigated using these lateral device structures provide key insights into BHJ materials and are complementary to studies performed on vertical solar cell structures. In this article, we present the first report using nanoscale lithographically defined in situ voltage probes to study the potential profile in an active lateral BHJ device. Additionally, we correlate these measurements with transport simulations of lateral BHJ devices as well as confocal microscopy measurements that enable the estimation of carrier mobilities and recombination mechanisms.

**Special Issue:** Paul F. Barbara Memorial Issue

**Received:** August 29, 2012
**Revised:** February 5, 2013

   dx.doi.org/10.1021/jp308594b | *J. Phys. Chem. B* XXXX, XXX, XXX−XXX

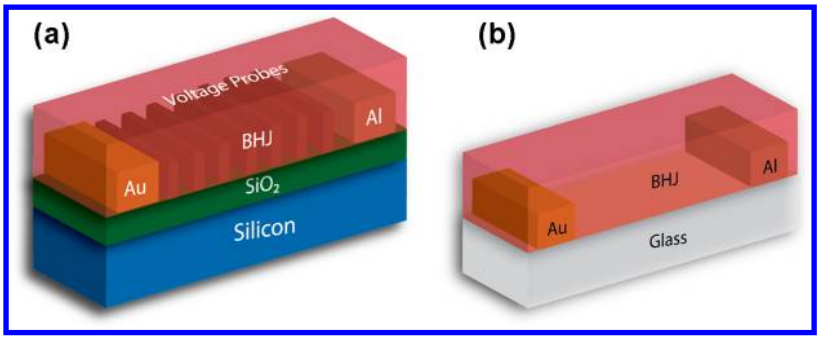


**Figure 1.** Schematic illustration of a lateral BHJ device used for (a) in situ potentiometry and (b) scanning confocal photocurrent microscopy.

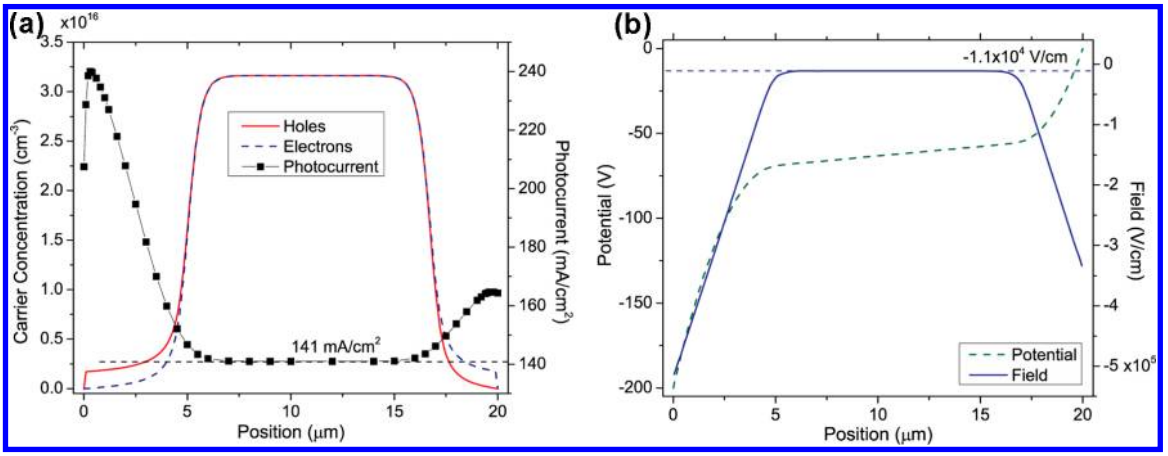


**Figure 2.** (a) Carrier concentration as a function of position (solid lines) for a numerically simulated 20 $\mu$m lateral BHJ device under uniform illumination. The dotted line shows the amount of collected photocurrent as a function of excitation position with a simulated laser spot with a fwhm of 0.5 $\mu$m as well as uniform illumination. (b) Simulated electric field and potential profile for the same 20 $\mu$m lateral BHJ device.

## 2. DEVICE THEORY AND NUMERICAL SIMULATIONS

The device physics of lateral BHJ devices represents a combination of photovoltaic and photoconductor physics as a result of the device geometry and mode of electrical operation. This combination of geometry and operational mode results in space-charge-limited device physics, which has been reported within OPV cells[11] as well as lateral BHJ devices.[12,13] Previous theoretical work predicts three transport zones where there is efficient carrier collection near (or within a drift length of) the two electrodes and a central region where very little photocurrent can be collected.[14] When there is significant asymmetry between electron and hole mobilities, one of the space charge regions (SCRs) becomes very small, and the device can be considered to be possessing two transport zones, one SCR and one recombination zone. Recently, Ooi et al. have simulated a lateral BHJ device that shows the presence of two transport regions, a SCR where there is an accumulation of the slower carrier (carrier with lower mobility) and a recombination zone where there is little net photogeneration and most carriers recombine.[13] This simulation solves Poisson's equation as well as the drift/diffusion under appropriate boundary values to determine the carrier concentration of electrons and holes as well as the electric field and potential profile throughout the device. Full details of the numerical simulation can be found within the aforementioned reference.

In order to simulate a device with two SCRs and a central recombination zone, the asymmetry in carrier mobilities was reduced (from a factor of 10 as in previous simulations), and the simulation was run for a 20 $\mu$m lateral BHJ device where the electron mobility ($\mu_e$) was $1.5 \times 10^{-3}$ cm$^2$/V*s, the hole mobility ($\mu_h$) was $1.0 \times 10^{-3}$ cm$^2$/V*s, an applied reverse bias of 200 V, a generation rate of ($G$) $1.0 \times 10^{21}$ cm$^{-3}$/s, and a bimolecular recombination coefficient ($k_{BI}$) of $1.0 \times 10^{-12}$ cm$^2$/s. The anode for hole extraction is located at $x = 0$ $\mu$m, and the cathode for electron extraction is located at $x = 20$ $\mu$m. Electrical contacts were modeled as noninjecting and with no barrier for carrier extraction. The resulting carrier concentration as a function of position is shown in Figure 2a, and the electric field and potential profile is shown in Figure 2b. Within Figure 2a, areas of unipolar carrier accumulation occur next to each electrode; holes accumulate near the anode and electrons near the cathode. The accumulation of charge carriers occurs within a few micrometers of each electrode because carriers are transported into this region more quickly than they can be extracted. If the potential drop in the recombination zone is small, then the $J-V$ characteristics of the entire device can be described by eq 1

$$J_{photo} = (4\varepsilon\mu)^{1/4}(qG)^{3/4}V^{1/2} \quad (1)$$

where $\varepsilon$ is the dielectric constant, $\mu$ is the mobility of the slower carrier, $q$ is the elementary charge, and $V$ is the applied voltage. Within the central zone, both electrons and holes are present in approximately equal populations, and most of these carriers recombine. This is a result of a small (but nonzero) electric field present within this central region, which is more than an order of magnitude smaller than within the adjacent SCRs. Carriers within the recombination zone should follow ohmic $J-V$ characteristics.


dx.doi.org/10.1021/jp308594b | J. Phys. Chem. B XXXX, XXX, XXX−XXX

By comparing the carrier concentration profile (Figure 2a) and the potential profile (Figure 2b), the extents of the SCRs can be determined in multiple ways. Areas with asymmetric carrier densities are characteristic of SCRs, while areas with high symmetric carrier densities are present within the recombination zone. Similarly, within the SCRs, there is a roughly linear decrease in electric field when moving away from the electrode with a smaller constant electric field within the recombination zone. Transitions between the SCRs and the recombination zone can be demarcated by large changes in carrier concentration, electric field, or the slope of the potential profile and net photogeneration rate.

In addition to simulations of lateral BHJ devices with uniform illumination and applied bias, we also simulated an experiment based on nonuniform illumination, which is useful to researchers who would like to spatially resolve transport parameters within BHJ materials. This has been demonstrated recently with an experimental method called scanning confocal photocurrent microscopy (SCPM), which utilizes common confocal microscopy tools.[12] SCPM measurements have been used to determine the size of the SCRs with a lateral BHJ device under various biasing and illumination conditions. The total photocurrent of the same 20 $\mu$m lateral BHJ device was simulated for a laser spot with a fwhm of 0.5 $\mu$m at many discrete points along the transport channel. The total collected photocurrent as a function of excitation position is shown as the discrete points in Figure 2a. The areas of high collected photocurrent correspond to the extents of the SCRs adjacent to each electrode. Between the SCRs, there is a greatly reduced amount of photocurrent being collected as the laser excitation occurs within the recombination zone, and most of the photogenerated charges recombine. For laser excitation within the recombination zone, the total simulated photocurrent is 141 mA/cm$^2$. This is the same value as for simulations that only have uniform illumination and no position-dependent laser excitation. This confirms that in an ideal system, any photogenerated carriers within the recombination zone recombine and do not contribute to the overall net photocurrent within a lateral BHJ device.

## 3. EXPERIMENTAL METHODS

Lateral bulk heterojunction devices for DC characterization and in situ potentiometry, illustrated in Figure 1a, were fabricated on a p-type silicon substrate with 2600 Å of thermally grown silicon dioxide. Interdigitated electrodes and voltage probes were defined using a JEOL JBX-6000 electron beam lithography tool in three separate steps. The device channel lengths ranged from 100 nm to 20 $\mu$m with a $W/L$ = 1000. For in situ potentiometry samples, 25 Ni probes extended 60 $\mu$m into the channel and were 200 nm wide with an average spacing of 600 nm. Aluminum (Al) was used for the cathodes, gold (Au) for the anodes, and nickel (Ni) for the voltage probes and device pads. Al and Au were deposited under vacuum using thermal evaporation, while Ni was deposited under vacuum using electron beam evaporation. All metal layers were deposited to a thickness of 500 Å.

Before the deposition of the BHJ layer, the substrate was dipped into a phosphoric acid solution for 10 s to remove any aluminum oxide on the surface of the Al electrodes. This was followed by a solvent rinse procedure to degrease the substrate, which consisted of acetone, methanol, and isopropyl alcohol. The BHJ absorber layer was deposited from a 20 mg/mL solution of P3HT/PCBM (1:1 by weight) in chloroform that had been heated to 50 °C and stirred for over 16 h. The BHJ was spun-cast at 1200 rpm for 60 s and then annealed at 140 °C for 15 min in a nitrogen atmosphere.

Electrical measurements were performed in a Desert Cryogenics cryogenic probe station under vacuum better than $5 \times 10^{-3}$ Torr at 300 K using an Agilent 4155C semiconductor parameter analyzer. Current versus voltage characteristics were measured with the gate disconnected in the dark as well as under illumination. In situ potentiometry was performed simultaneously with the current versus voltage measurements using the Ni probes in the channel. Sample illumination was achieved using an Oriel model 66912 and 66907 150 W ozone-free xenon lamp. The optical spectrum was modified using an AM1.5 spectral filter, and the light intensity was 100 mW/cm$^2$. Neutral density filters were used to attenuate the incident light to four different intensities ranging from 20 to 100 mW/cm$^2$.

Lateral BHJ devices for SCPM, illustrated in Figure 1b, were fabricated on a glass substrate in a manner similar to the sample used for in situ potentiometry, including electrode fabrication and cleaning prior to BHJ coating. The device length was 15 $\mu$m with $W/L$ = 50. The BHJ absorber layer was deposited from a 12 mg/mL solution of PSBTBT/$C_{71}$–PCBM (1:2 by weight) dissolved in dichlorobenzene that was heated to 120 °C for more than 24 h. The BHJ was spun-cast on the prepared substrates at 1000 rpm for 60 s, and this was followed by encapsulation and annealing at 120 °C for 10 min in a nitrogen atmosphere.

SCPM image maps were obtained using an Ar ion laser selected at 514 nm for excitation, which was focused through an extra long working distance 60× magnification Nikon objective. The size of the focal spot was estimated to be ~600 nm in diameter, as determined by scanning across a step edge in a patterned metal film. For sample scanning capabilities, a Physik Instrumente (PI) piezoelectric stage (model E-501.00) was mounted onto a Nikon Diaphot 300 inverted microscope. The excitation beam was chopped at 140 Hz using a Thorlabs Optical Chopper (Model MC2000). The photocurrent flowing in the lateral BHJ device was amplified using a Stanford Research Systems model SR570 low noise current preamplifier and measured using a Stanford Research Systems model SR830 lock-in amplifier. The fluorescence and reflectance were collected simultaneously using a 50/50 beam splitter and two microphoton devices (MPDs). The lateral BHJ devices were biased using a Keithley 6430 sub-femtoamp remote source meter. White light illumination was provided using the quartz tungsten halogen microscope illuminator provided with the Nikon Diaphot 300 inverted microscope and had an intensity of 150 mW/cm$^2$.

## 4. RESULTS AND DISCUSSION

**4.1. Photocurrent versus Device Length.** Photocurrent versus device length from P3HT/PCBM lateral BHJ devices with lengths ranging from 100 nm to 20 $\mu$m were measured under AM1.5 illumination at various reverse bias conditions and are shown in Figure 3. The photocurrent increases as a function of reverse bias as well as of device length until the device length reaches about 5 $\mu$m. This is expected as most carriers that are photogenerated in the SCRs will be efficiently extracted and will contribute to photocurrent within the device. As the size of the SCRs has been previously shown to be 2–5 $\mu$m in these materials under the stated experimental conditions,[12] increases in device length up to this point should contribute to additional extracted photocurrent. As the device


dx.doi.org/10.1021/jp308594b | J. Phys. Chem. B XXXX, XXX, XXX–XXX

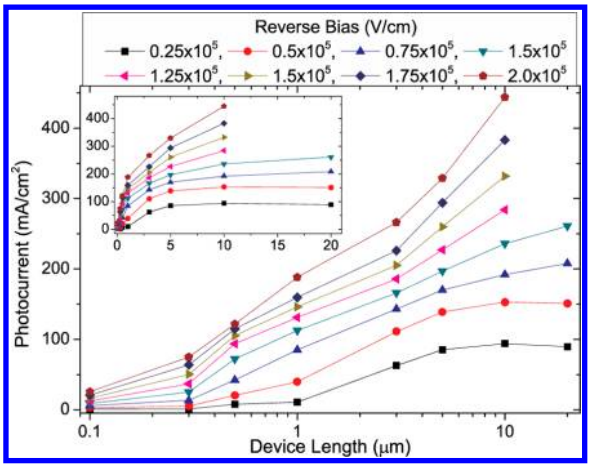


**Figure 3.** Photocurrent versus device length (log scale) for P3HT/PCBM lateral BHJ devices. (Inset) Photocurrent versus device length (linear scale) for the same devices.

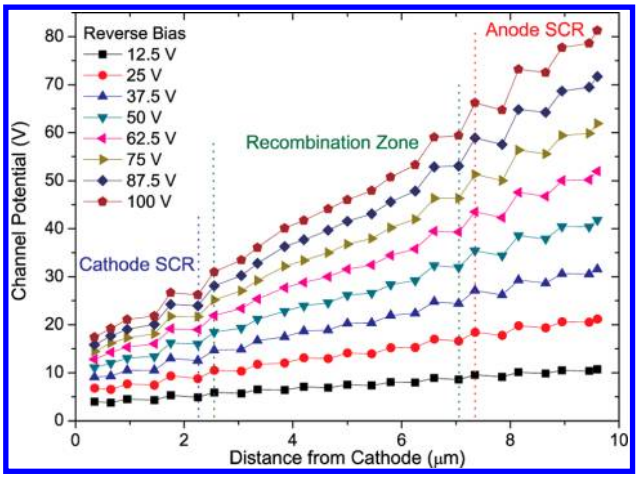


**Figure 4.** Channel potential versus position in the channel for a 10 $\mu$m P3HT/PCBM lateral BHJ device measured by in situ potentiometry. The extents of the SCRs and the recombination zone have been labeled.

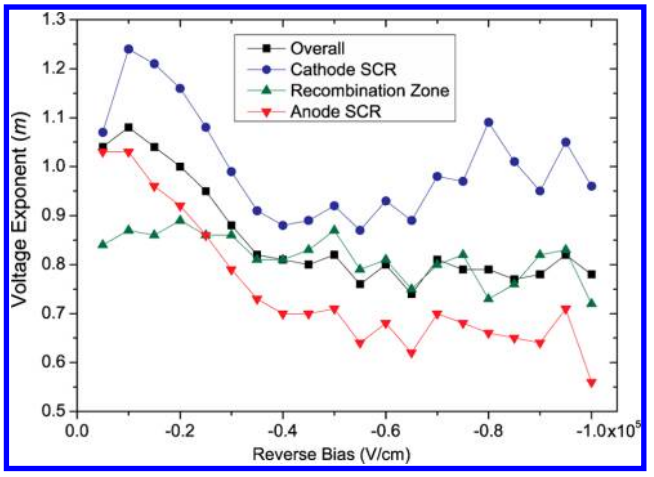


**Figure 5.** Voltage exponent versus reverse bias electric field for the same 10 $\mu$m P3HT/PCBM lateral BHJ device.

length continues to increase, only the length of the recombination zone (and not the SCRs) increases, and very few additional carriers will exit the device and contribute to photocurrent. This transit length characteristics is shown in the inset of Figure 3, where the device length is plotted on a linear scale. As the device length increases beyond 5 $\mu$m, the photocurrent flowing in the BHJ device saturates due to few additional photogenerated carriers contributing to the photocurrent. The trends present in the photocurrent versus device length data support the existence of three transport regions, and their characteristics are described in the theory section.

**4.2. In Situ Potentiometry.** The use of multiple in situ voltage probes throughout the channel gives us a direct method to monitor the potential profile at many points along the device. A 10 $\mu$m lateral BHJ device with P3HT/PCBM as an active layer and 25 in situ voltage probes has been used to characterize the transport and recombination regimes present within BHJ materials. As described in the theory section, measuring the potential profile within a lateral BHJ device can yield the size of the SCRs as well as the size of the recombination zone by determining where the slope of the potential profile changes. The potential profile under several reverse bias conditions is shown in Figure 4. The changes in the slope of the potential profile at approximately 2.5 and 7 $\mu$m from the cathode are indicative of boundaries between the two SCRs and the central recombination zone. However, further analysis of the current versus voltage data is needed to determine the exact region lengths as the $J-V$ characteristics of a region between any two voltage probes (or probe and electrode) can be calculated separately.

The $J-V$ characteristics in the recombination zone are expected to be ohmic, whereas in the SCRs, they should be more complex. We define the size of the SCRs and the recombination zone from the spatial extent of these different $J-V$ characteristics within the channel. To determine the voltage exponent $m$, where $J \propto V^m$, the functional form of the resulting current versus voltage drop in each transport region is determined using previously published methods.[11,12] The voltage exponent as a function of electric field in each transport region as well as the applied electric field across the entire lateral BHJ device is shown in Figure 5.

At electric field strengths less than $0.4 \times 10^5$ V/cm, the voltage exponent is high as a result of electronic barriers for carrier extraction. Similar barriers for carrier injection have been well reported for organic TFTs and OLEDs. At electric field strengths greater than $0.4 \times 10^5$ V/cm, the voltage exponent for the SCR adjacent to the anode drops to a value between 0.6 and 0.7. The voltage exponent for the SCR adjacent to the cathode also drops below its extraction limited value with increasing electric field, and the trends in the data are similar to those for the anode SCR. This SCR behavior is observed in the region from the cathode to 2.3 $\mu$m within the channel and in the region 7.3 $\mu$m within the channel to the anode. The location of the cathode is defined as the origin. From these data, the size of the SCR adjacent to the cathode is therefore $2.3 \pm 0.4$ $\mu$m, and for the SCR adjacent to the anode is $2.7 \pm 0.4$ $\mu$m, with uncertainty due to the thickness and spacing of the voltage probes. These results have been recorded in Table 1.

Within the recombination zone, ohmic current versus voltage characteristics are expected ($J \propto V$), and voltage exponent values between 0.75 and 0.9 are seen. This ohmic exponent behavior is observed in the region from 3.1 to 7.1 $\mu$m within the channel. The resulting length of the recombination zone is then $5.0 \pm 0.8$ $\mu$m. When the voltage exponents for the SCRs and the recombination zone are calculated over larger regions


dx.doi.org/10.1021/jp308594b | J. Phys. Chem. B XXXX, XXX, XXX−XXX

**Table 1. Lateral Extent of the SCRs for Various BHJ Materials**

| | P3HT/PCBM | | PSBTBT/PCBM[12] | | PSBTBT/$C_{71}$-PCBM | |
|---|---|---|---|---|---|---|
| applied field (V/cm) | cathode SCR ($\mu$m) | anode SCR ($\mu$m) | cathode SCR ($\mu$m) | anode SCR ($\mu$m) | cathode SCR ($\mu$m) | anode SCR ($\mu$m) |
| $0.5 \times 10^5$ | 2.3 | 2.7 | 3.7 | 3.7 | | |
| $0.66 \times 10^5$ | | | | | 2.1 | 1.5 |
| $0.75 \times 10^5$ | | | 4.1 | 4.5 | | |
| $1.0 \times 10^5$ | | | 4.9 | 4.9 | 4.7 | 1.5 |
| $1.3 \times 10^5$ | | | | | 5.5 | 1.5 |

of the channel, their behavior with respect to the electric field becomes less distinct. This indicates that the analyzed regions include parts of both the SCRs and the recombination zone. We can therefore be confident that we determine the true extent of the SCRs within the channel using this voltage exponent method. The discrepancies in the measured versus theoretical values of the voltage exponent can be attributed to the uncertainty in where exactly the gradual transition between space-charge-limited transport and ohmic transport occurs. Also, the extracted lengths of the SCRs and the recombination zone are assumed to be independent of the electric field for calculation of the voltage exponent. In reality, the size of the SCRs increases with increases in the applied bias, which leads to more uncertainty within the length measurements. When the voltage exponent of the total device is characterized, the contact effects present within the SCRs at low field are also present. At increased bias, the total voltage exponent exhibits a character that resembles the recombination zone. This is to be expected as the voltage exponent of the composite device would be a combination of all three zones, with the recombination zone encompassing greater than 50% of the device length. Calculations show that the ratio of the two SCR lengths correlate directly with the mobility ratio of the carriers. The approximately equal SCR lengths are an indication of nearly balanced electron and hole mobilities.

The recombination zone, in lateral BHJ devices, is an ideal geometry to study material properties of the BHJ layer as it is free from interface effects related to the electrodes. Within the recombination zone, there is no net photogeneration; therefore, $U = G \propto P$, where $U$ is the recombination rate and $P$ is the incident light intensity. The conductivity in the recombination zone is $\sigma = q(\Delta n \mu_e + \Delta p \mu_h)$, where $\Delta n$ and $\Delta p$ are the electron and hole concentrations, respectively. As shown in Figure 2a, the electron and hole concentrations are equal in the recombination zone; therefore, the conductivity reduces to $\sigma = q\Delta n(\mu_e + \mu_h)$. Bimolecular recombination has been discussed in many reports to be the predominant recombination mechanism within BHJ materials.[15−19] For bimolecular recombination, the recombination rate is related to both the electron and the hole populations (which are equal); therefore, $U \propto \Delta n^2$. Because the conductivity is proportional to the carrier concentration, for bimolecular recombination, the square of the conductivity should be proportional to the light intensity, $\sigma^2 \propto P$. Figure 6 shows the square of the conductivity in the recombination zone as a function of incident light intensity. The linear relationship between the square of the conductivity and the incident light intensity that shows that bimolecular recombination is present and confirmed within P3HT:PCBM, which is consistent with previous reports.[18,20]

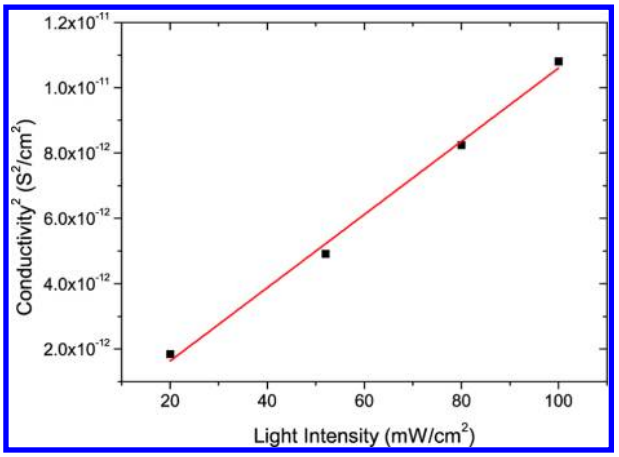


**Figure 6.** Square of the conductivity within the recombination zone versus light intensity for the same 10 $\mu$m P3HT/PCBM lateral BHJ device.

**4.3. Scanning Confocal Photocurrent Microscopy.** SCPM was used to spatially map the laser-induced photocurrent within the BHJ layer of a PSBTBT/$C_{71}$−PCBM device. The technique utilizes a piezoelectric stage, in which an electronic device is raster-scanned across a chopped focused laser beam and the photocurrent is collected at each pixel, producing an image of the generated photocurrent. This technique has been used to study Si,[21] $Cu(In_{1-x}Ga_x)Se_2$,[22] nanoparticle devices,[23] and organic photovoltaics.[24,25] These studies lead to an understanding of charge collection as a function of morphology and can be coupled to other optical techniques, such as fluorescence, in order to achieve chemical-specific information. Information from SCPM measurements on lateral BHJ devices gives the optical response as a function of distance from the electrodes and is expected to show two photocurrent peaks (one at each electrode) as the laser is scanned from the cathode to the anode, with a recombination zone in the center. Figure 7a shows a typical SCPM image of a 15 $\mu$m device under a 150 mW/cm$^2$ white light bias, with a 100 V reverse bias. A photocurrent peak adjacent to cathode can be seen decaying a few micrometers into the center of the channel. Figures 7b and c show the same image at a reverse bias of 150 and 200 V, respectively. With increasing bias, the photocurrent peak increases in height and extends farther inward, while a second peak grows at the other electrode, the anode. Cross sections of the device under a reverse bias of 100, 150, and 200 V are shown in Figure 7d, in which the line scans were averaged across the entire device in order to quantify the SCR regions. The analysis of the SCR regions is reported elsewhere;[12] briefly, the peaks were modeled to a single exponential, $J \propto \exp(-x/L_C')$ for electrons and $J \propto \exp((x - L)/L_A')$ for holes, where $L_C$ is the size of the SCR at the cathode and $L_A$ is the SCR of the anode. Furthermore, the peaks do not appear at the electrodes due to the finite diameter of the laser spot and must be corrected in the analysis. Correcting for the instrument broadening, the SCR region becomes $L_C = (L_{C'}^2 + (1.4\ \mu m)^2)^{1/2}$ for the cathode, and likewise, $L_A = (L_{A'}^2 + (1.4\ \mu m)^2)^{1/2}$ for the anode. Fitting the data, shown in red in Figure 7d, it was found that the SCRs adjacent to the cathode are 2.10, 4.71, and 5.50 $\mu$m for an applied reverse bias of 100, 150, and 200 V, respectively. The length of the SCR adjacent to the anode was found to be 1.45, 1.47, and 1.48 $\mu$m. The size of the SCR region increases with increasing bias for the accumulated


dx.doi.org/10.1021/jp308594b | J. Phys. Chem. B XXXX, XXX, XXX−XXX

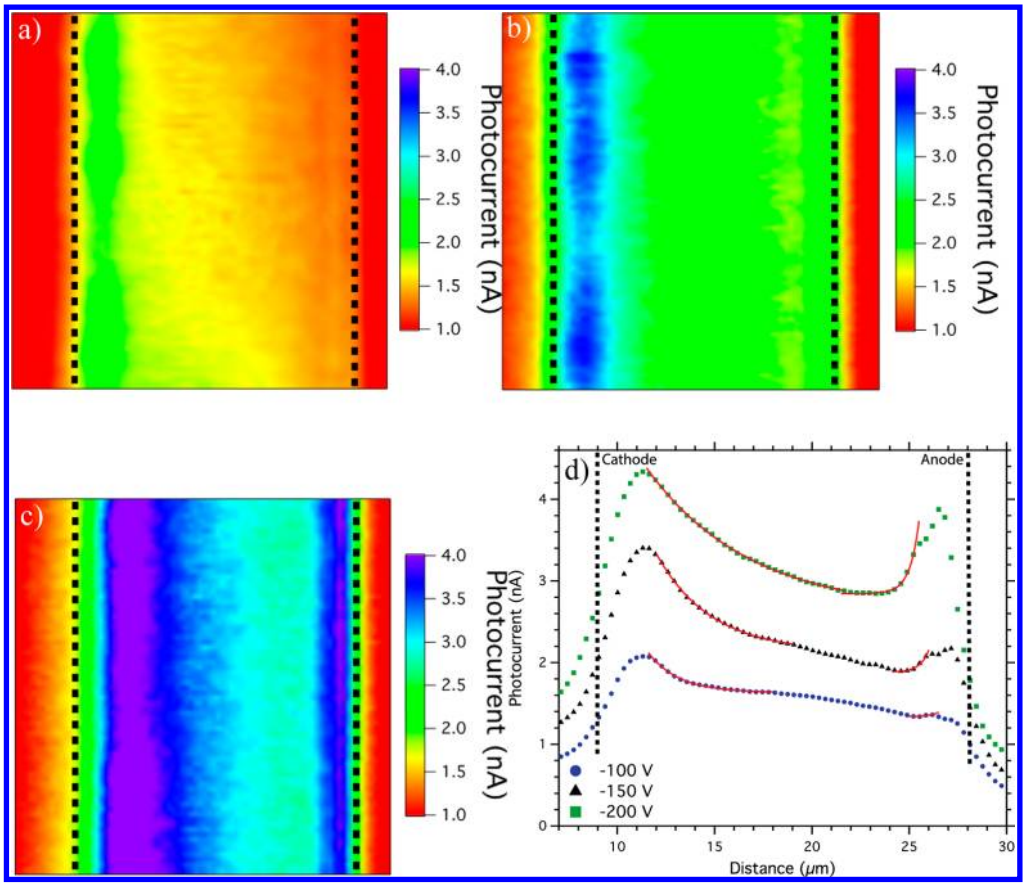


**Figure 7.** Photocurrent maps taken from a 15 $\mu$m PSBTBT/$C_{71}$–PCBM lateral BHJ device under 150 mW/cm$^2$ white light bias with an externally applied reverse bias of (a) 100, (b) 150, and (c) 200 V. (d) Extracted photocurrent profiles (dots) and data fits (red lines) to extract the SCR lengths from the same lateral BHJ device. Photocurrent maps are 32 $\mu$m × 32 $\mu$m.

holes, and furthermore, we show that the SCR for accumulated holes is much greater than that for accumulated electrons for this device. The results of the SCPM with PSBTBT/$C_{71}$–PCBM are shown in Table 1.

Past work has shown that under white light bias with a PSBTBT/PCBM ($C_{61}$) device, the SCRs for electrons and holes were nearly equal (also included in Table 1).[12] However, we have shown that replacing the acceptor with $C_{71}$–PCBM greatly increases the transit lengths of holes, but the electron transport length greatly diminishes. However, it is found that the overall device performance of a vertical cell is enhanced with $C_{71}$–PCBM, which we attribute to a greater absorption in the visible wavelengths.[26] On the basis of Mihailetchi et al.'s results,[11] we believe that using BHJ materials with matched electron and hole mobilities will result in OPV cells with increased power conversion efficiencies compared to those devices that have highly asymmetric carrier mobilities, and SCPM is a technique that allows evaluation of such mobility balance. However, we also observed that vertical cells employing $C_{71}$–PCBM perform better than those with $C_{61}$–PCBM (even though the latter has better mobility matching), which we attribute to the greater absorption of visible light by $C_{71}$–PCBM.

## 5. CONCLUSION

Lateral BHJ devices provide a platform to examine how BHJ materials behave in regimes that mimic solar operation as well as regimes that are useful to study bulk material properties. Photocurrent versus device length measurements have shown that as the device length increases beyond the length of the SCRs adjacent to both electrodes, a recombination zone forms and behaves as predicted by numerical simulations. The size of the SCRs as well as the recombination zone can be measured by both in situ potentiometry as well as SCPM and is tabulated in Table 1. Carriers that are photogenerated within the SCRs do not easily recombine and contribute to the steady-state photocurrent, whereas carriers that are photogenerated within the recombination zone typically recombine do not add any additional photocurrent to the device. The size of the SCRs is related to the mobility and lifetime of charge carriers and is an important parameter for characterizing BHJ materials for use in OPV cells. Currently, the size of the SCRs allows the calculation of carrier mobilities only in particular situations, yet ongoing work is being performed to enable researchers to use these techniques to quantify the mobility of charge carriers in most settings. Measurements performed in the recombination zone reveal bulk recombination properties where the mechanism of recombination is shown to be bimolecular. Although many of these measurements have previously been performed in other geometries and device structures, the lateral BHJ device structure allows for material and device parameters to be determined through the use of steady-state experimental procedures under conditions similar to those for conventional solar cell operation. The simplicity and utility of the techniques presented in this article should be advantageous to OPV material producers and device manufacturers.


dx.doi.org/10.1021/jp308594b | J. Phys. Chem. B XXXX, XXX, XXX–XXX

## AUTHOR INFORMATION

### Notes

The authors declare no competing financial interest.

## ACKNOWLEDGMENTS

The authors would like to thank Konarka Technologies for access to PSBTBT. This material is based upon work supported as part of the program "Understanding Charge Separation and Transfer at Interfaces in Energy Materials (EFRC:CST)", an Energy Frontier Research Center funded by the U.S. Department of Energy, Office of Science, Office of Basic Energy Sciences under Award Number DE-SC0001091. We gratefully acknowledge the leadership of the late Paul Barbara, the founding director of the EFRC-CST. E. Danielson would like to acknowledge the ONR under STTR project No. 00014-10-M-0317 and M. Glaz would like to acknowledge the NSF IGERT program (DGE-054917) for financial support. Z. Ooi acknowledges funding provided by A*STAR under the visiting investigator program (VIP).

## REFERENCES

(1) Clarke, T. M.; Peet, J.; Denk, P.; Dennler, G.; Lungenschmied, C.; Mozer, A. J. Non-Langevin Bimolecular Recombination in a Silole-Based Polymer:PCBM Solar Cell Measured by Time-Resolved Charge Extraction and Resistance-Dependent Time-of-Flight Techniques. *Energy Environ. Sci.* **2012**, *5* (1), 5241−5245.

(2) Morfa, A. J.; Nardes, A. M.; Shaheen, S. E.; Kopidakis, N.; van de Lagemaat, J. Time-of-Flight Studies of Electron-Collection Kinetics in Polymer:Fullerene Bulk-Heterojunction Solar Cells. *Adv. Funct. Mater.* **2011**, *21* (13), 2580−2586.

(3) Clarke, T. M.; Rodovsky, D. B.; Herzing, A. A.; Peet, J.; Dennler, G.; DeLongchamp, D.; Lungenschmied, C.; Mozer, A. J. Significantly Reduced Bimolecular Recombination in a Novel Silole-Based Polymer:Fullerene Blend. *Adv. Energy Mater.* **2011**, *1* (6), 1062−1067.

(4) Pivrikas, A.; Neugebauer, H.; Sariciftci, N. S. Charge Carrier Lifetime and Recombination in Bulk Heterojunction Solar Cells. *IEEE J. Sel. Top. Quantum Electron.* **2010**, *16* (6), 1746−1758.

(5) MacKenzie, R. C. I.; Shuttle, C. G.; Chabinyc, M. L.; Nelson, J. Extracting Microscopic Device Parameters from Transient Photocurrent Measurements of P3HT:PCBM Solar Cells. *Adv. Energy Mater.* **2012**, *2* (6), 662−669.

(6) Maurano, A.; Shuttle, C. G.; Hamilton, R.; Ballantyne, A. M.; Nelson, J.; Zhang, W.; Heeney, M.; Durrant, J. R. Transient Optoelectronic Analysis of Charge Carrier Losses in a Selenophene/Fullerene Blend Solar Cell. *J. Phys. Chem. C* **2011**, *115* (13), 5947−5957.

(7) Leong, W. L.; Cowan, S. R.; Heeger, A. J. Differential Resistance Analysis of Charge Carrier Losses in Organic Bulk Heterojunction Solar Cells: Observing the Transition from Bimolecular to Trap-Assisted Recombination and Quantifying the Order of Recombination. *Adv. Energy Mater.* **2011**, *1* (4), 517−522.

(8) Li, J. V.; Nardes, A. M.; Liang, Z.; Shaheen, S. E.; Gregg, B. A.; Levi, D. H. Simultaneous Measurement of Carrier Density and Mobility of Organic Semiconductors Using Capacitance Techniques. *Org. Electron.* **2011**, *12* (11), 1879−1885.

(9) Coffey, D. C.; Larson, B. W.; Hains, A. W.; Whitaker, J. B.; Kopidakis, N.; Boltalina, O. V.; Strauss, S. H.; Rumbles, G. An Optimal Driving Force for Converting Excitons into Free Carriers in Excitonic Solar Cells. *J. Phys. Chem. C* **2012**, *116* (16), 8916−8923.

(10) Rance, W. L.; Ferguson, A. J.; McCarthy-Ward, T.; Heeney, M.; Ginley, D. S.; Olson, D. C.; Rumbles, G.; Kopidakis, N. Photoinduced Carrier Generation and Decay Dynamics in Intercalated and Non-intercalated Polymer:Fullerene Bulk Heterojunctions. *ACS Nano* **2011**, *5* (7), 5635−5646.

(11) Mihailetchi, V. D.; Wildeman, J.; Blom, P. W. M. Space-Charge Limited Photocurrent. *Phys. Rev. Lett.* **2005**, *94* (12), 126602/1−126602/4.

(12) Lombardo, C. J.; Glaz, M. S.; Ooi, Z.-E.; Vanden Bout, D. A.; Dodabalapur, A. Scanning Photocurrent Microscopy of Lateral Organic Bulk Heterojunctions. *Phys. Chem. Chem. Phys.* **2012**, *14* (38), 13199−13203.

(13) Ooi, Z. E.; Chan, K. L.; Lombardo, C. J.; Dodabalapur, A. Analysis of Photocurrents in Lateral-Geometry Organic Bulk Heterojunction Devices. *Appl. Phys. Lett.* **2012**, *101* (5), 053301/1−053301/5.

(14) Goodman, A. M.; Rose, A. Double Extraction of Uniformly Generated Electron−Hole Pairs from Insulators with Noninjecting Contacts. *J. Appl. Phys.* **1971**, *42* (7), 2823−2830.

(15) Koster, L. J. A.; Mihailetchi, V. D.; Blom, P. W. M. Bimolecular Recombination in Polymer/Fullerene Bulk Heterojunction Solar Cells. *Appl. Phys. Lett.* **2006**, *88* (5), 052104/1−052104/3.

(16) Mozer, A. J.; Dennler, G.; Sariciftci, N. S.; Westerling, M.; Pivrikas, A.; Österbacka, R.; Juska, G. Time-Dependent Mobility and Recombination of the Photoinduced Charge Carriers in Conjugated Polymer/Fullerene Bulk Heterojunction Solar Cells. *Phys. Rev. B* **2005**, *72* (3), 035217/1−035217/10.

(17) Pivrikas, A.; Juscaronka, G.; Mozer, A. J.; Scharber, M.; Arlauskas, K.; Sariciftci, N. S.; Stubb, H.; Osterbacka, R. Bimolecular Recombination Coefficient as a Sensitive Testing Parameter for Low-Mobility Solar-Cell Materials. *Phys. Rev. Lett.* **2005**, *94* (17), 176806/1−176806/4.

(18) Shuttle, C. G.; Hamilton, R.; O'Regan, B. C.; Nelson, J.; Durrant, J. R. Charge-Density-Based Analysis of the Current−Voltage Response of Polythiophene/Fullerene Photovoltaic Devices. *Proc. Natl. Acad. Sci. U.S.A.* **2010**, *107* (38), 16448−16452.

(19) Cowan, S. R.; Banerji, N.; Leong, W. L.; Heeger, A. J. Charge Formation, Recombination, and Sweep-Out Dynamics in Organic Solar Cells. *Adv. Funct. Mater.* **2012**, *22* (6), 1116−1128.

(20) Pivrikas, A.; Sariciftci, N. S.; Juška, G.; Österbacka, R. A Review of Charge Transport and Recombination in Polymer/Fullerene Organic Solar Cells. *Prog. Photovoltaics* **2007**, *15* (8), 677−696.

(21) Carstensen, J.; Popkirov, G.; Bahr, J.; Föll, H. CELLO: An Advanced LBIC Measurement Technique for Solar Cell Local Characterization. *Sol. Energy Mater. Sol. Cells* **2003**, *76* (4), 599−611.

(22) Ostrowski, D. P.; Glaz, M. S.; Goodfellow, B. W.; Akhavan, V. A.; Panthani, M. G.; Korgel, B. A.; Vanden Bout, D. A. Mapping Spatial Heterogeneity in $Cu(In_{1-x}Ga_x)Se_2$ Nanocrystal-Based Photovoltaics with Scanning Photocurrent and Fluorescence Microscopy. *Small* **2010**, *6* (24), 2832−2836.

(23) Strasfeld, D. B.; Dorn, A.; Wanger, D. D.; Bawendi, M. G. Imaging Schottky Barriers and Ohmic Contacts in PbS Quantum Dot Devices. *Nano Lett.* **2012**, *12* (2), 569−575.

(24) Brenner, T. J. K.; McNeill, C. R. Spatially Resolved Spectroscopic Mapping of Photocurrent and Photoluminescence in Polymer Blend Photovoltaic Devices. *J. Phys. Chem. C* **2011**, *115* (39), 19364−19370.

(25) Bull, T. A.; Pingree, L. S. C.; Jenekhe, S. A.; Ginger, D. S.; Luscombe, C. K. The Role of Mesoscopic PCBM Crystallites in Solvent Vapor Annealed Copolymer Solar Cells. *ACS Nano* **2009**, *3* (3), 627−636.

(26) Pfuetzner, S.; Meiss, J.; Petrich, A.; Riede, M.; Leo, K. Improved Bulk Heterojunction Organic Solar Cells Employing $C_{70}$ Fullerenes. *Appl. Phys. Lett.* **2009**, *94* (22), 223307/1−223307/3.